nature geoscience

Article

https://doi.org/10.1038/s41561-024-01514-1

Gold nugget formation from earthquake-induced piezoelectricity in quartz

Received: 12 September 2023

Accepted: 22 July 2024

Published online: 2 September 2024

Check for updates

Christopher R. Voisey [1] ✉, Nicholas J. R. Hunter[1,2], Andrew G. Tomkins[1], Joël Brugger [1], Weihua Liu [3], Yang Liu [4] & Vladimir Luzin [5]

Gold nuggets occur predominantly in quartz veins, and the current paradigm posits that gold precipitates from dilute (<1 mg kg^{-1} gold), hot, water ± carbon dioxide-rich fluids owing to changes in temperature, pressure and/or fluid chemistry. However, the widespread occurrence of large gold nuggets is at odds with the dilute nature of these fluids and the chemical inertness of quartz. Quartz is the only abundant piezoelectric mineral on Earth, and the cyclical nature of earthquake activity that drives orogenic gold deposit formation means that quartz crystals in veins will experience thousands of episodes of deviatoric stress. Here we use quartz deformation experiments and piezoelectric modelling to investigate whether piezoelectric discharge from quartz can explain the ubiquitous gold–quartz association and the formation of gold nuggets. We find that stress on quartz crystals can generate enough voltage to electrochemically deposit aqueous gold from solution as well as accumulate gold nanoparticles. Nucleation of gold via piezo-driven reactions is rate-limiting because quartz is an insulator; however, since gold is a conductor, our results show that existing gold grains are the focus of ongoing growth. We suggest this mechanism can help explain the creation of large nuggets and the commonly observed highly interconnected gold networks within quartz vein fractures.

Ore deposits represent natural enrichments of elements compared with their normal distribution in Earth's crust. Gold deposits stand out by having the highest degree of enrichment, by factors of 10^3 to 10^4 required to make economic deposits (4–40 ppm gold), compared with base metals, such as copper, that require ~200× enrichment. Gold nuggets represent the most extreme examples of this gold enrichment. Most nuggets originate from the quartz veins formed in orogenic gold systems found around the world. These systems have had exceptional economic importance throughout human history, representing up to 75% of all gold ever mined[1].

In orogenic gold systems, gold-bearing hydrothermal fluids from the mid- to lower crust are transported along fracture networks by seismic ruptures associated with regional collisional tectonics[2,3]. These systems are hosted in rocks of variable metamorphic grade involving mid- to upper-crustal conditions between 200 °C and 650 °C and 1–5 kbar (100–500 MPa)[4,5]. The pervasive occurrence of crack–seal microstructures in quartz-carbonate veining found in these deposits indicates formation from hundreds to thousands of episodic fluid infiltration events, each associated with separate earthquakes[2,3]. The cyclic nature of these seismic events means that fractures are

[1]School of Earth, Atmosphere and Environment, Monash University, Melbourne, Victoria, Australia. [2]Centre for Health Systems Development, Australian Institute of Primary Care and Ageing, La Trobe University, Bundoora Campus, Melbourne, Victoria, Australia. [3]CSIRO Mineral Resources, Clayton, Victoria, Australia. [4]Monash Centre for Electron Microscopy, Monash University, Melbourne, Victoria, Australia. [5]Australian Centre for Neutron Scattering, ANSTO, Sydney, New South Wales, Australia. ✉e-mail: chris.voisey@monash.edu

https://doi.org/10.1038/s41561-024-01514-1

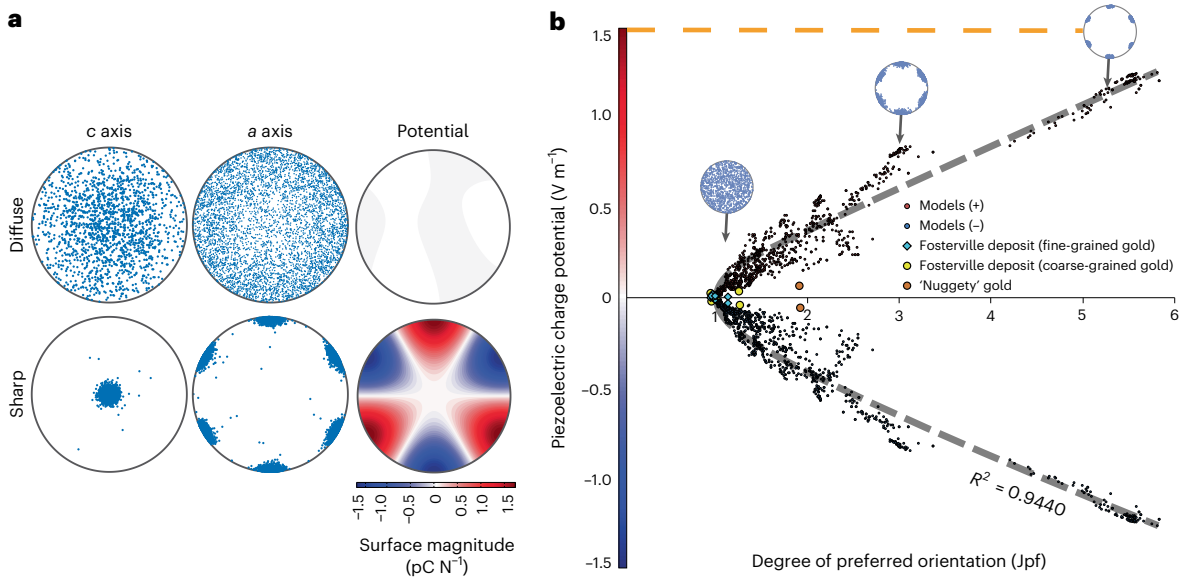

Fig. 1 | Quartz crystal models depicting the relationship between a CPO ('texture') and piezoelectric polarization. a, Top: when {*a*} axis orientations are uniformly distributed, the tensor exhibits very poor polarization. Bottom: conversely, where a strong preferred orientation is present in the quartz {*a*} axes, the piezoelectric tensor is highly polarized. **b**, Integrated piezoelectric potentials of models and samples measured using neutron diffraction. Here, the degree of preferred orientation is quantified using the pole figure index (Jpf). The dashed orange line represents the experimentally calibrated potential for a quartz single crystal.

periodically opened and filled with fluids, resulting in spatially focused quartz–gold vein systems[6–8].

At the mineral system scale, the overall mechanisms responsible for the transport and deposition of gold are relatively well understood, resulting from an interplay between geochemical and structural factors. Geochemists have focused on causes of fluid chemistry changes to explain gold deposition, whereas structural geologists have focused on physical mechanisms driving fluid flow. However, the formation of large native gold accumulations in orogenic quartz veins remains enigmatic. They represent a long-unsolved paradox: the solubility of gold in fluids is up to ~1 ppm (ref. 9), whereas the local concentration of gold in quartz can greatly exceed 50%, occasionally producing nuggets and masses of gold–quartz reef weighing tens to hundreds of kilograms (10 kg Au requires 10 million kg H_2O, equivalent to five Olympic swimming pools). The formation of gold nanoparticles has been offered as a solution because it represents a way to exceed this solubility constraint[10,11], but we still lack a clear mechanism that would cause billions of nanoparticles to accumulate in one place preferentially. In other gold deposit types, such as epithermal deposits, 'bonanza'-grade gold ore results from stable boiling of fluids near the surface. This mechanism leaves a clear textural and geochemical signature that cannot be applied to most orogenic deposits since sustained boiling is not possible below ~2 km depth[12]. Here, we show that piezoelectric discharge from quartz crystals may provide a suitable explanation for extreme gold enrichment in orogenic quartz veins.

The piezoelectric effect of quartz

Quartz is the only common mineral that forms crystals lacking a centre of symmetry ('non-centrosymmetric'). Non-centrosymmetric crystals distorted under stress have an imbalance in their internal electric configuration, which produces an electrical potential—or voltage—across the crystal that is directly proportional to the applied mechanical force[13] (Extended Data Fig. 1). This anisotropy that arises in the internal electrical configuration of the crystal is referred to as piezoelectricity and is one of the strongest examples of electrical polarization in nature[14]. It has even been suggested that 'earthquake lightning' (ball lightning observed pre, syn and post rupture) is due to piezoelectricity in Earth's crust[15] and that the electromagnetic response may be utilized to predict impending earthquake events[16].

Quartz veins have been shown to emit a measurable piezoelectric charge when a mechanical stress is applied[17–19], and this is enhanced where there is preferred orientation of the crystals[14]. Deformation of materials with distinct preferred orientation produces strong directional variation in piezoelectric polarization, due to favourable alignment of the electric poles[20]. Crack–seal type quartz veins associated with orogenic gold deposits typically exhibit strong crystallographic orientations due to growth competition between adjacent crystals[6,7]. Figure 1a shows the quartz *a* axes of two model specimens in three-dimensional space: the axes on the top specimen are strongly oriented, whereas the axes on the bottom are random. The corresponding piezoelectric tensors (Fig. 1b) reveal that the top specimen exhibits strong anisotropic electrical polarization, whereas the bottom specimen does not.

To examine this phenomenon in natural gold-bearing quartz veins, samples from the Fosterville deposit (Victoria, Australia; Extended Data Fig. 2) were collected and measured using neutron diffraction to evaluate their crystallographic texture and corresponding piezoelectric properties (Methods). Figure 1b shows the textures and calculated piezoelectric tensors of these samples. Overall, both modelling and texture analyses show that piezoelectric polarization of quartz veins from orogenic gold deposits was typically ~0.01 V m^{-1}, and a maximum of 0.03 V m^{-1} in nuggety samples. A key point is that the piezoelectric potential of bulk rocks is always much less than that of a single quartz crystal (1.92 V m^{-1}; Fig. 1b, dashed orange line). This means that a polycrystalline rock will never match the piezoelectric potential of a single quartz crystal, even those with a strongly aligned texture. Therefore, piezoelectric effects will be localized at the surfaces of crystals ideally oriented with respect to an imposed stress direction. Thus, we further explore the piezoelectric behaviour of single quartz crystals.

Piezocatalytic chemistry

The electric field established by a strained piezoelectric material affects the electronic properties both inside and outside the material. In an insulator, such as quartz, no charge can freely move to counteract the

https://doi.org/10.1038/s41561-024-01514-1

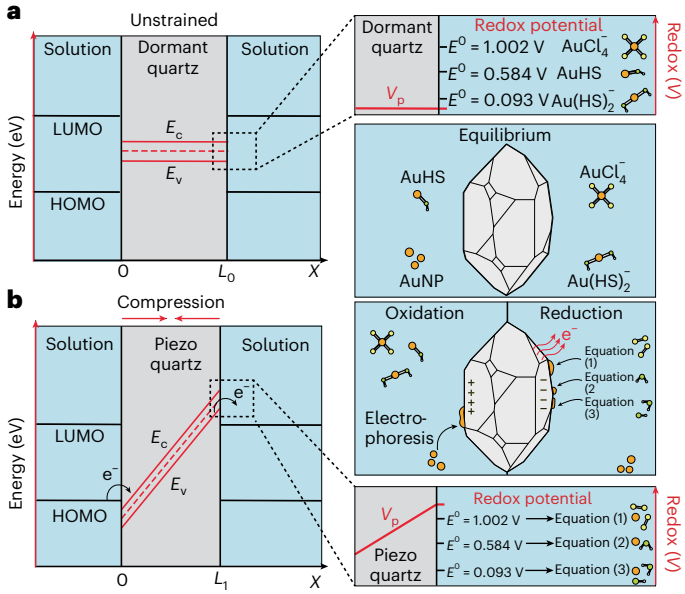

Fig. 2 | Summary of gold accumulation by the quartz piezocatalysis model. LUMO, lowest occupied molecular orbit of a chemical species in solution; HOMO, highest occupied molecular orbit of a chemical species in solution. Oxidation removes electrons from HOMO, and reduction adds electrons to LUMO. Conduction (E_c) and valence (E_v) bands of quartz act as the reservoirs for electrons to be donated or accepted from molecules in solution. *X* axis is displacement of the quartz crystal width in arbitrary units. **a**, Quartz crystal is unstrained at neutral width (L_0) and in equilibrium with the surrounding solution. Quartz valence and conduction bands are not shifted, and the piezoelectric potential (V_p) is zero. **b**, Compressive strain has shortened the quartz crystal (L_1), shifting the energy state of occupied (valence band) and unoccupied (conduction band) states across the quartz crystal. This energy difference is the piezoelectric potential (V_p). This allows electron transfer out of the valence band and into the surrounding solution (fluid reduction). Moreover, it allows electron transfer into the conduction band from the surrounding solution (fluid oxidation). Piezoelectric potential (V_p) exceeds the redox potential of Au ligands and leads to the electrochemical reduction of Au by equations (1)–(3). AuNPs are adhered onto cathodic surfaces by electrophoresis (see text for discussion). Modified from Starr et al.[21].

piezoelectric field and the electric field that is generated linearly shifts the energy of occupied (valence band) and unoccupied (conduction band) states across the material (Fig. 2)[21]. This shift within the material disturbs the distribution of free charges between the material surface and any adjacent medium, such as a surrounding solution. The interactions of any free-moving particles that carry a charge (for example, electrons, ions and/or nanoparticles) depend on the electronic states between the material and solution[22–24]. The difference between the energy levels of the oxidizing or reducing agents in the solution (that is, their redox potential) and the conduction/valence bands of the piezoelectric solid can be considered a potential barrier that electrons must overcome for reaction to proceed[25,26]. In this way, the deformation of a piezoelectric material by an external stress causes a shift in this potential barrier, leading to the flow of electrons from the material's surface to species in solution, or vice versa (Fig. 2). A piezoelectric material that is continuously alternated between tensile and compressive strains results in a varying electric field that prevents equilibrium with its environment, allowing the enduring exchange of charge between the material and surrounding solution. This exchange is referred to as piezocatalysis and can drive electrochemical reactions at the material–solution interface[27–29]. We experimentally examined this concept to demonstrate piezocatalytic chemical reactions on the surface of quartz submerged in gold-bearing aqueous solutions.

Piezoelectric deposition of gold

Our experiments were conducted using 12 slabs of quartz cut from natural crystals, 6 of which were used as controls (Methods). The slabs were placed within sealed chambers containing gold-bearing aqueous solutions and were strained by application of a linear actuator, which mechanically oscillated at a fixed frequency and amplitude at ambient conditions (Extended Data Fig. 3). To best replicate seismic waves from a natural earthquake (thousands of which cumulatively form orogenic gold deposits), a frequency of 20 Hz was chosen. Large earthquakes generally have frequencies between 0.01 and 10 Hz, whereas smaller earthquakes, like those associated with aftershocks on subsidiary faults that host gold deposits[30], commonly have frequencies between 5 and 60 Hz (ref. 31). To test whether gold would deposit from fluids with either (1) dissolved gold complexed with hydrosulfide and chloride ligands or (2) colloidal gold nanoparticles[9], a duplicate series of experiments was conducted using solutions containing each. The first series consisted of two bare single-crystal quartz slabs. In the second series, 2 nm of iridium was coated onto two single-crystal slabs to expedite the rate of piezo-electrochemical exchange. The final series used natural polycrystalline quartz vein samples containing native gold grains. In each case, the control samples were prepared the same way and subjected to the same solutions but lacked an oscillatory stress.

The dissolved gold experiments used a solution containing 75 ppm gold introduced as $HAuCl_4$ in a NaCl–H_2O solvent (Methods). Gold is present predominantly as $AuCl_4^-$ in this solution. Although the dominant gold-bearing ligands in natural orogenic gold systems are $Au(HS)_2^-$ and $Au(HS)^0$, these compounds are poorly soluble at room temperature and unsuitable for this experiment[32]. Importantly, the reduction potential of $AuCl_4^-$ is much larger than that of $Au(HS)_2^-$ or $Au(HS)^0$ (refs. 33,34), so if $AuCl_4^-$ is reduced by quartz piezocatalysis, it follows that hydrosulfide compounds can be as well (equations (1)–(3)) (Extended Data Fig. 4).

$$AuCl_4^- + 3e^- \rightarrow Au + 4Cl^- \qquad E^0 = 1.002\,V \qquad (1)$$

$$Au(HS)^0 + H^+ + e^- \rightarrow Au + H_2S \qquad E^0 = 0.548\,V \qquad (2)$$

$$Au(HS)_2^- + H^+ + e^- \rightarrow Au + H_2S + HS^- \qquad E^0 = 0.093\,V \qquad (3)$$

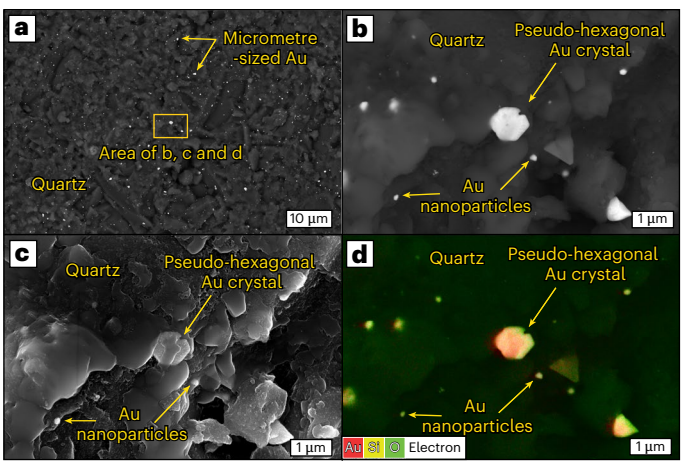

Fig. 3 | Results from the uncoated quartz gold chloride ($AuCl_4$) experiment. **a**, BSE image of the quartz surface exhibiting distribution of gold particles deposits from $AuCl_4$ solution. Pseudocrystalline nanocrystals can be seen. **b**,**c**, BSE (**b**) and SE (**c**) images of the square area outlined in **a**. **d**, EDS image of the square area in **a** highlighting the chemistry of sample area. BSE, backscattered electron; SE, secondary electron; EDS, energy-dispersive spectroscopy.

https://doi.org/10.1038/s41561-024-01514-1

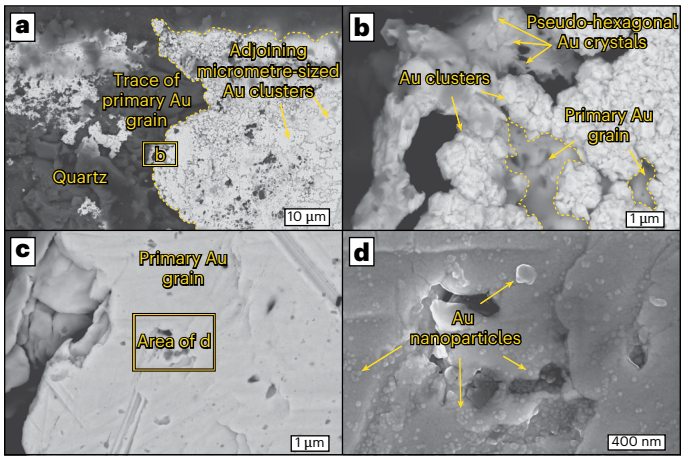

Fig. 4 | Results from the gold chloride ($AuCl_4$) and gold nanoparticle (AuNP) with natural auriferous quartz experiments. a, BSE image of a native gold grain in quartz extensively coated by micrometre-sized clusters of Au. Preferential deposition of gold from solution onto the conductive native gold grain, and not onto the insulating quartz, can be seen. **b**, BSE image of the square area outlined in **a**. **c**, BSE image of a native gold grain. **d**, SE image of the area outlined in **c** showcasing AuNP deposition onto the native gold grain surface. BSE, backscattered electron; SE, secondary electron; EDS, energy-dispersive spectroscopy.

The crystal slabs were submerged in 75 ml of solution and deformed for 1 h. Figure 3 shows that numerous gold grains were deposited on the bare quartz surface, while the control quartz slab hosted no detectable gold (Extended Data Fig. 5). This indicates that the energy shift of the quartz valence band was sufficient to electrochemically reduce gold from solution by equation (1). Most of the deposited gold particles are 1 µm or smaller and are commonly pseudocrystalline structures. On the natural gold-bearing quartz sample, abundant 1–2-µm-sized gold clusters and pseudo-hexagonal crystals have grown onto the primary gold grain with little deposition on the quartz surface (Fig. 4a,b). The Ir-coated sample shows gold grains ranging from 100 to 200 nm in size, which are commonly conjoined or form linear arrays (Extended Data Fig. 6). In each case, the control samples lacked these features (Extended Data Figs. 7 and 8). Nanocrystal formation and linear arrays are both consistent with the early stages of diffusion-limited aggregation (DLA)[35], where non-bonded particles cluster together to reduce free energy, which leads to transitory structures that radiate from a point or a line (Figs. 3 and 4 and Extended Data Fig. 6). The DLA process is common in electrodeposition reactions[36], whereby particles suspended in a fluid migrate under the effects of an electric field and deposit onto electrodes. We suggest that, upon piezocatalytic reduction from solution by equation (1), newly formed gold particles are electrodeposited onto the sample surface with preference towards pre-existing gold that acts as an electrode by utilizing the piezoelectric bias (Fig. 4). Once deposited, gold forms transitory nanocrystals and grows into arrays by electric field-induced DLA. Similar structures associated with DLA have been reported in natural gold deposits, such as in Nevada and California[37,38].

The colloidal gold experiments were conducted using a solution containing 95 ppm of gold nanoparticles (2–20 nm diameter) in a S–Cl solvent stabilized by colloidal silica (Methods). The quartz slabs were submerged in 75 ml of solution and deformed for 1 h. Figure 5 shows that numerous gold nanoparticles accumulated on the quartz surface with a prominent cluster up to 1–2 µm in size. Figure 4c,d shows numerous gold nanoparticles adhering to the primary gold surface, reaching sizes up to ~120 nm. The Ir-coated sample shows abundant clusters on the scale of 5–8 µm (Extended Data Fig. 9). For each experiment, the controls yielded no result (Extended Data Figs. 5, 8 and 10).

Gold nanoparticles may remain in suspension indefinitely unless their 'aggregation barrier' is overcome, each behaving as a charged particle repelling one another[39]. Our observation of gold clusters on the quartz and gold surfaces indicates that this aggregation barrier has been overcome through the piezoelectric effect (Fig. 5). Given the piezoelectric property of quartz, gold nanoparticles are predicted to have been adsorbed at sites with ideal electrochemical potential (that is, the instantaneous cathodic surface), by electrostatic attraction and/or electrophoresis. This can effectively seed the surface with conductive gold nuclei, and then subsequent pulses of charging cause the nuclei to grow. Production of nanoparticle clusters and attachment to gold surfaces is expected in electrochemical deposition processes since crystal growth often predominates nucleation, leading to the formation of large clusters without complete coverage of the surface[40].

Piezoelectric gold accumulation in orogenic deposits

We have shown that single quartz crystals have the highest piezoelectric potential when compared with bulk rock volumes, which explains the localization and then growth of gold into nuggets within veins, as opposed to widely dispersed gold atoms. During any given strain event, the highest voltage within a veined volume of rock will be developed within ideally oriented quartz crystals in veins. The most productive use of this voltage will be where conducting materials, such as existing gold particles, are present. The cyclical nature of seismicity that creates orogenic gold deposits means that these quartz veins form and repeatedly fracture incrementally, experiencing numerous episodes of deviatoric stress during their growth[41]. Since orogenic deposits are hosted by secondary and tertiary fault structures[42], they are the focus of tens of thousands of earthquake aftershocks during their formation, each event lasting seconds to several minutes[43]. Aftershocks form clusters and can maintain permeability on aftershock-hosting faults for extended periods of time, with reactivation of these same structures[43]. This setting is ideal for maintaining infiltration of auriferous fluids through fractured quartz veins that are experiencing syn-shock strain. The elastic rattling of quartz crystals within veins during seismic activity leads to oscillations of the oxidation–reduction reaction fronts on either side of quartz crystal surfaces (Fig. 2). We have experimentally shown that even modest strain on bare quartz crystals can generate piezoelectric potentials capable of reducing gold-bearing ligands—$AuCl_4^-$ and moreover $Au(HS)_2^-$ and $Au(HS)^0$—causing gold to

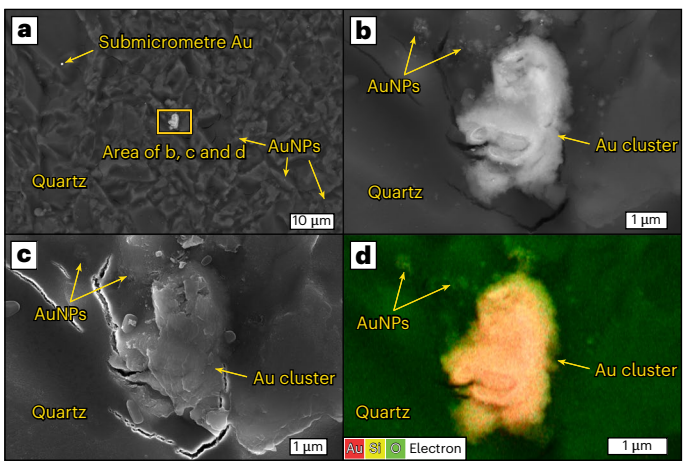

Fig. 5 | Results from the uncoated quartz gold nanoparticle (AuNP) experiment. a, BSE image of AuNPs on the quartz surface exhibiting localized clustering. **b**, BSE image of the area outlined in **a**. **c**, SE image of the square area outlined in **a**. **d**, EDS image of the square area in **a** highlighting the chemistry of sample area. BSE, backscattered electron; SE, secondary electron; EDS, energy-dispersive spectroscopy.

be electrochemically deposited (Figs. 2 and 3). We have also shown that if the fluid contains any gold nanoparticles, these will be preferentially adsorbed onto quartz surfaces acting as electrodes and grow during deformation (Figs. 2 and 5). Since naked and conductive-coated piezoelectric materials perform consonantly when subjected to large strain (>0.1%) and comparably at moderate strain (>0.02%)[44], the quartz crystals that were made conductive through Ir coating yield results that could reflect natural strains developed during earthquakes (upwards of 3% in extreme cases) (Extended Data Figs. 6 and 9)[45].

Our experiments have shown (Fig. 4) that, because gold has excellent electrical conductance, existing gold grains will adopt the electrical bias from adjacent quartz crystals during deformation, allowing them to become the focus of ongoing piezoeletroplating as fluid infiltration is repeated many times. This can provide an explanation for the discrete occurrence of large gold accumulations, via low probability of nucleation of gold from natural undersaturated fluids, but an increasing probability of further deposition once a gold grain has nucleated. This may explain the nucleation and growth of large gold nuggets in orogenic gold systems, as opposed to other gold systems that can feature high grades but rarely contain large nuggets. Additionally, this provides interpretation for highly interconnected networks of gold along fractures within quartz veins; the fractures are repeatedly reactivated as fluid pathways, and since piezoelectric voltages are coupled with stress, the maximum achievable voltages occur during brittle failure. Since piezoelectric voltages are instantaneous and leave behind no visible tracer, this can rationalize why gold nuggets commonly appear to be 'floating' in quartz veins with no obvious chemical or physical trap. In this way, we suggest that piezoelectric gold accumulation could be a solution to the long-standing 'gold nugget paradox'.

Online content

Any methods, additional references, Nature Portfolio reporting summaries, source data, extended data, supplementary information, acknowledgements, peer review information; details of author contributions and competing interests; and statements of data and code availability are available at https://doi.org/10.1038/s41561-024-01514-1.

References

1. Phillips, N. in *Modern Approaches in Solid Earth Sciences* (eds Dilek, Y., Pirajno, F. & Windley, B.) 7–15 (Springer, 2022).
2. Sibson, R. H., Moore, J. M. & Rankin, A. H. Seismic pumping—a hydrothermal fluid transport mechanism. *J. Geol. Soc.* **131**, 653–659 (1975).
3. Cox, S. F. Faulting processes at high fluid pressures: an example of fault valve behavior from the Wattle Gully Fault, Victoria, Australia. *J. Geophys. Res. Solid Earth* **100**, 12841–12859 (1995).
4. Groves, D. I. The crustal continuum model for late-archaean lode-gold deposits of the Yilgarn Block, Western Australia. *Miner. Deposita* **28**, 366–374 (1993).
5. Tomkins, A. G. & Grundy, C. Upper temperature limits of orogenic gold deposit formation: constraints from the granulite-hosted Griffin's Find Deposit, Yilgarn Craton. *Econ. Geol.* **104**, 669–685 (2009).
6. Cox, S. F. & Etheridge, M. A. Crack–seal fibre growth mechanisms and their significance in the development of oriented layer silicate microstructures. *Tectonophysics* **92**, 147–170 (1983).
7. Ramsay, J. G. The crack–seal mechanism of rock deformation. *Nature* **284**, 135–139 (1980).
8. Renard, F., Gratier, J. P. & Jamtveit, B. Kinetics of crack-sealing, intergranular pressure solution, and compaction around active faults. *J. Struct. Geol.* **22**, 1395–1407 (2000).
9. Williams-Jones, A. E., Bowell, R. J. & Migdisov, A. A. Gold in solution. *Elements* **5**, 281–287 (2009).
10. Voisey, C. R. et al. Aseismic refinement of orogenic gold systems. *Econ. Geol.* **115**, 33–50 (2020).
11. Petrella, L. et al. Nanoparticle suspensions from carbon-rich fluid make high-grade gold deposits. *Nat. Commun.* **13**, 3795 (2022).
12. Williams, R. T. Coseismic boiling cannot seal faults: implications for the seismic cycle. *Geology* **47**, 461–464 (2019).
13. Curie, J. & Curie, P. Développement par compression de l'électricité polaire dans les Cristaux hémièdres à faces inclinées. *Bull. Soc. Minéral. France* **3**, 90–93 (1880).
14. Bishop, J. R. Piezoelectric effects in quartz-rich rocks. *Tectonophysics* **77**, 297–321 (1981).
15. Finkelstein, D. & Powell, J. Earthquake lightning. *Nature* **228**, 759–760 (1970).
16. Wang, J. H. Piezoelectricity as a mechanism on generation of electromagnetic precursors before earthquakes. *Geophys. J. Int.* **224**, 682–700 (2020).
17. Ghomshei, M. M. & Templeton, T. L. Piezoelectric and *a*-axes fabric along a quartz vein. *Phys. Earth Planet. Inter.* **55**, 374–386 (1989).
18. Parkhomenko, E. I. *Electrification Phenomena in Rocks* (Pleunum Press, 1971).
19. Murthy, Y. S. & Bhimasankaram, V. L. Experimental results of the piezoelectric activity of Quartzose Rocks. in *SEG Technical Program Expanded Abstracts* (Society of Exploration Geophysicists, 1985); https://doi.org/10.1190/1.1892893
20. Mainprice, D., Bachmann, F., Hielscher, R., Schaeben, H. & Lloyd, G. E. Calculating anisotropic piezoelectric properties from texture data using the MTEX open-source package. *Geol. Soc. Lond. Spec. Publ.* **409**, 223–249 (2014).
21. Starr, M. B. & Wang, X. Coupling of piezoelectric effect with electrochemical processes. *Nano Energy* **14**, 296–311 (2015).
22. Wang, Z. L. Piezopotential gated nanowire devices: piezotronics and piezo-phototronics. *Nano Today* **5**, 540–552 (2010).
23. Wang, Z. L. Progress in piezotronics and piezo-phototronics. *Adv. Mater.* **24**, 4632–4646 (2012).
24. Zhang, Y., Liu, Y. & Wang, Z. L. Fundamental theory of piezotronics. *Adv. Mater.* **23**, 3004–3013 (2011).
25. Gerischer, H. & Ekardt, W. Fermi levels in electrolytes and the absolute scale of redox potentials. *Appl. Phys. Lett.* **43**, 393–395 (1983).
26. Leblanc, S. E. & Fogler, H. S. The role of conduction/valence bands and redox potential in accelerated mineral dissolution. *AlChE J.* **32**, 1702–1709 (1986).
27. Hong, K.-S., Xu, H., Konishi, H. & Li, X. Direct water splitting through vibrating piezoelectric microfibers in water. *J. Phys. Chem. Lett.* **1**, 997–1002 (2010).
28. Hong, K.-S., Xu, H., Konishi, H. & Li, X. Piezoelectrochemical effect: a new mechanism for azo dye decolorization in aqueous solution through vibrating piezoelectric microfibers. *J. Phys. Chem. C* **116**, 13045–13051 (2012).
29. Starr, M. B., Shi, J. & Wang, X. Piezopotential-driven redox reactions at the surface of piezoelectric materials. *Angew. Chem. Int. Ed.* **51**, 5962–5966 (2012).
30. Cox, S. F. & Ruming, K. The St Ives Mesothermal Gold System, Western Australia—a case of golden aftershocks? *J. Struct. Geol.* **26**, 1109–1125 (2004).
31. Tosi, P., Sbarra, P. & De Rubeis, V. Earthquake sound perception. *Geophys. Res. Lett.* **39**, 24 (2012).
32. Pokrovski, G. S., Akinfiev, N. N., Borisova, A. Y., Zotov, A. V. & Kouzmanov, K. Gold speciation and transport in geological fluids: Insights from experiments and physical–chemical modelling. *Geol. Soc. Lond. Spec. Publ.* **402**, 9–70 (2014).
33. Bard, A. J., Parsons, R. & Jordan, J. *Standard Potentials in Aqueous Solution* (Routledge, 2017).
34. Maddox, L. M., Bancroft, G. M., Scaini, M. J. & Lorimer, J. W. Invisible gold; comparison of au deposition on pyrite and arsenopyrite. *Am. Mineral.* **83**, 1240–1245 (1998).

35. Liu, D., Zhou, W., Song, X. & Qiu, Z. Fractal simulation of flocculation processes using a diffusion-limited aggregation model. *Fractal Fract.* **1**, 12 (2017).
36. Witten, T. A. & Sander, L. M. Diffusion-limited aggregation, a kinetic critical phenomenon. *Phys. Rev. Lett.* **47**, 1400–1403 (1981).
37. Saunders, J. A. & Schoenly, P. A. Boiling, colloid nucleation and aggregation, and the genesis of bonanza Au–Ag ores of the Sleeper Deposit, Nevada. *Miner. Deposita* **30**, 199–210 (1995).
38. Monecke, T. et al. Natural growth of gold dendrites within silica gels. *Geology* **51**, 189–192 (2023).
39. Polte, J. Fundamental growth principles of colloidal metal nanoparticles—a new perspective. *CrystEngComm* **17**, 6809–6830 (2015).
40. Roustom, B. E., Fóti, G. & Comninellis, C. Preparation of gold nanoparticles by heat treatment of sputter deposited gold on boron-doped diamond film electrode. *Electrochem. Commun.* **7**, 398–405 (2005).
41. Robert, F., Boullier, A.-M. & Firdaous, K. Gold–quartz veins in metamorphic terranes and their bearing on the role of fluids in faulting. *J. Geophys. Res. Solid Earth* **100**, 12861–12879 (1995).
42. Goldfarb, R. J., Groves, D. I. & Gardoll, S. Orogenic gold and geologic time: a global synthesis. *Ore Geol. Rev.* **18**, 1–75 (2001).
43. Micklethwaite, S., Sheldon, H. A. & Baker, T. Active fault and shear processes and their implications for mineral deposit formation and discovery. *J. Struct. Geol.* **32**, 151–165 (2010).
44. Starr, M. B. & Wang, X. Fundamental analysis of piezocatalysis process on the surfaces of strained piezoelectric materials. *Sci. Rep.* **3**, 2160 (2013).
45. Trepmann, C. A. & Stöckhert, B. Short-wavelength undulatory extinction in quartz recording coseismic deformation in the middle crust—an experimental study. *Solid Earth* **4**, 263–276 (2013).

Methods

Neutron diffraction analysis

Neutron diffraction was used to characterize the typical crystallographic preferred orientation (CPO) of auriferous quartz veins. We used representative samples from the Fosterville gold deposit in Victoria, which has been previously described[46]. The sample was cut into a 2 cm^3 cube aligned parallel with the fault trace and parallel to slickenside striations, and subsequently measured using the constant wavelength neutron diffractometer KOWARI at the Australian Nuclear Science and Technology Organisation (ANSTO, Lucas Heights, Australia).

We used an incident neutron beam with a maximum cross-section of 35 × 60 mm^2 and a constant neutron wavelength of 2.5 Å to study the sample. Diffraction peaks were collected using a two-dimensional position-sensitive area detector at three incremental angles, each comprising 13° to 14° of detector coverage. The resulting diffraction patterns were fitted with Gaussian peaks and polynomial functions to resolve overlapping and reduce background noise. The full pole figures of the detected reflections at each position were then transferred to 3° × 3° grid meshes.

We generated CPO data, in the form of lower-hemispheric pole figures, by calculating the orientation density function of the sample. Orientation density functions were constructed using a 'de la Vallee Poussin' kernel with 5° halfwidth.

Piezoelectric modelling

Tensorial modelling was used to calculate the total piezoelectric potential (V m^{-1}) of a hypothetical 2 cm^3 cubic specimen of pure polycrystalline quartz and with variable grain size and degrees of CPO. Piezoelectric potentials for a given specimen are determined by calculating the piezoelectric strain tensor of the texture. This method has been detailed for quartz[14].

Grains within each specimen were modelled as ellipses with an aspect ratio of 1.5 and grain sizes between 0.1 and 10 mm. Thus, for the given specimen dimensions and grain size ranges, a model comprised anywhere between 15 and 15^{19} quartz grains. A total of 1,100 models were run.

Modelling was undertaken using the open-source software package MTEX (https://mtex-toolbox.github.io) and following the script of ref. 20. The degree of preferred orientation in each model was described quantitatively using the *J* index[47]. The piezoelectric potential (Pz) associated with each model was measured as the maximum positive and negative magnitudes in the resulting piezoelectric tensor.

Preparation of gold solutions

Hydrothermal fluids that form orogenic gold deposits are H_2O–CO_2 rich with intermediate fO_2, 3–7 wt% NaCl and circum-neutral pH of 5.5 (ref. 48). Hydrogen sulfide complexes are the dominant ligands for gold transportation in hydrothermal fluids that form orogenic deposits[9]; however, due to the instability of these complexes at room temperature, we opted to use the $AuCl_4$ ligand (see text in the section 'Piezoelectric deposition of gold')[32]. Additionally, it has recently been suggested that orogenic deposits form from gold nanoparticles in suspension[10,11]. Therefore, we have also prepared a solution with colloidal gold to test both hypotheses.

The Au–NaCl–H_2O-based gold solution was prepared using $HAuCl_4 \times xH_2O$ salt. The following reagents were weighed using an analytical balance: NaCl (5.8431 g), $HAuCl_4$ (0.0047 g) and H_2O (200 g). This results in a solution with 75 ppm gold and a pH of 4.4 that is stable indefinitely (>1 year) at room temperature. The N_2S-based gold colloidal solutions were prepared using a method described in previous experimental studies[49]. One-hundred grams of 0.50 millimolal Au(III) chloride solution was heated to 70–80 °C, then ~2.0 g of 25 millimolal Na_2S solutions was added with vigorous stirring. Colloidal silica (LUDOX AM30, particle size ~12 nm, diluted to 0.9–1.5 wt% SiO_2) was added to the gold colloid solutions and found to stabilize the Na_2S-based gold colloid solutions for several weeks at room temperature. Although natural gold solutions are known to contain 100 ppb to 1 ppm of gold[9], we have chosen higher gold concentrations to increase the chance of observing the result by scanning electron microscopy (SEM) since only 75 ml of solution was used per experiment. Considering the stability of each solution, the gold concentration has no effect on whether piezoelectricity was responsible for destabilizing them. It is important to note that each experiment was conducted within 24 h of the solutions being prepared.

Preparation of single-crystalline quartz slabs

Quartz crystals were obtained from a gem dealer and were cut into two 2-cm-long, 1-cm-wide and 0.5-cm-high slabs. The slabs were prepared such that they are parallel to the *x* axis and perpendicular to the *y* axis; this allows for mechanical stress to be applied towards the *x* axis, leaving an {*m*} face exposed for electrochemical reaction. A duplicate of each quartz slab, cut from the same crystal in the same orientation, was prepared as a control for each of the six experiments. Two nanometres of iridium was coated onto the surface of four of the quartz slab samples as a conductive layer to allow accurate voltage measurements by oscilloscope. To accommodate for the low strain (~0.003595%) generated by our apparatus, these coated quartz samples were also used to expedite piezoelectrochemical reactions in two experiments aiming to mimic high-strain events. This is due to coated piezoelectric materials behaving analogously to uncoated ones experiencing relatively large magnitudes of strain (>0.1%)[44]. It should be noted that conductive coating does not change the voltage generated.

Deformation experiment

The voltage output of the quartz slabs was first characterized in air by a digital oscilloscope. Voltage outputs between 0.4 and 1.4 V were obtained and varied on the basis of the pressure applied by a linear actuator, where higher pressure led to higher voltage. For both experiments, the linear actuator mechanically oscillated with a fixed frequency of 20 Hz and applied a pressure of 275 kPa directly onto the quartz slabs for the maximum voltage output of ~1.4 V. For each experiment, the quartz slab would be placed within a sealed chamber and submerged in 75 ml of their respective solution and deformed by the actuator for 1 h at room temperature. Although individual earthquakes last seconds to minutes, orogenic deposits form cumulatively from hundreds to thousands of these events. A duration of 1 h was chosen to simulate multiple events occurring on one quartz surface to gain insight into the nature of gold growth. The control quartz slabs were submerged in the same volume of the same Au-bearing solution(s) for the entire experiment duration, but not stressed. Upon completion, the slabs were removed from the sample chamber and dried by an air blow gun.

SEM

Imaging and energy-dispersive spectroscopy of the quartz slabs was conducted at the Monash Centre for Electron Microscopy (Victoria, Australia) using a Thermo Scientific Helios 5 UX FIB-SEM. The quartz slabs were coated with 2 nm of iridium and mounted upon a large stub holder using carbon tape. A 15 kV accelerating voltage and 0.10 nA beam current were used to acquire images of all samples. Aztec software was used for the construction of energy-dispersive spectroscopy maps.

Data availability

Neutron diffraction measurements of quartz samples and associated data used to model the piezoelectric properties are available via figshare at https://doi.org/10.6084/m9.figshare.26315281 (ref. 50). All other data supporting the findings of this study (sample images and geochemical models) are available within the article and its extended data files.

Code availability

The code used for piezoelectric potential tensorial modelling can be found in ref. 20.

References

46. Hunter, N. J. R. et al. Deformation mechanisms in orogenic gold systems during aseismic periods: microstructural evidence from the central Victorian gold deposits, Southeast Australia. *Econ. Geol.* **116**, 1849–1864 (2021).
47. Bunge, H.-J. *Texture Analysis in Materials Science: Mathematical Methods* (Elsevier, 1982).
48. Goldfarb, R. J. & Groves, D. I. Orogenic gold: common or evolving fluid and metal sources through time. *Lithos* **233**, 2–26 (2015).
49. Liu, W. et al. Colloidal gold in sulphur and citrate-bearing hydrothermal fluids: an experimental study. *Ore Geol. Rev.* **114**, 103142 (2019).
50. Voisey, C. Piezo_properties.xlsx. *figshare* https://doi.org/10.6084/m9.figshare.26315281 (2024).

Acknowledgements

This study is supported by Australian Research Council (LP200200897) and MRIWA project M10412 awarded to A.G.T., J.B. and W.L. We acknowledge the use of instruments and scientific and technical assistance at the Monash Centre for Electron Microscopy (MCEM), Monash University, the Victorian Node of Microscopy Australia. This research used equipment funded by Australian Research Council grant: Thermo Fisher Scientific Helios 5 UX FIB-SEM ARC Funding (LE200100132). We thank Agnico Eagles Mines Limited and the staff at Fosterville Gold Mine for providing samples and site access. We thank Y. Xing and D. Willis for assistance and discussions throughout the project.

Author contributions

C.R.V. conceptualized the project, designed and conducted piezoelectric laboratory experiments and was lead writer of the paper. N.J.R.H. processed and interpreted neutron diffraction data, constructed relevant figures and helped write the paper. A.G.T. helped conceptualize the project and interpretation. J.B. helped design the aqueous experiments and solutions and constructed geochemical models. W.L. designed and created the nanoparticle suspensions. Y.L. conducted SEM and energy-dispersive spectroscopy. V.L. conducted the neutron diffraction experiments. All authors reviewed the paper before submission.

Competing interests

The authors declare no competing interests.

Additional information

Extended data is available for this paper at https://doi.org/10.1038/s41561-024-01514-1.

Correspondence and requests for materials should be addressed to Christopher R. Voisey.

Peer review information *Nature Geoscience* thanks David Groves, Mark Hannington, Randolph Williams and Yanhao Yu for their contribution to the peer review of this work. Primary Handling Editor: Alison Hunt, in collaboration with the *Nature Geoscience* team.

https://doi.org/10.1038/s41561-024-01514-1

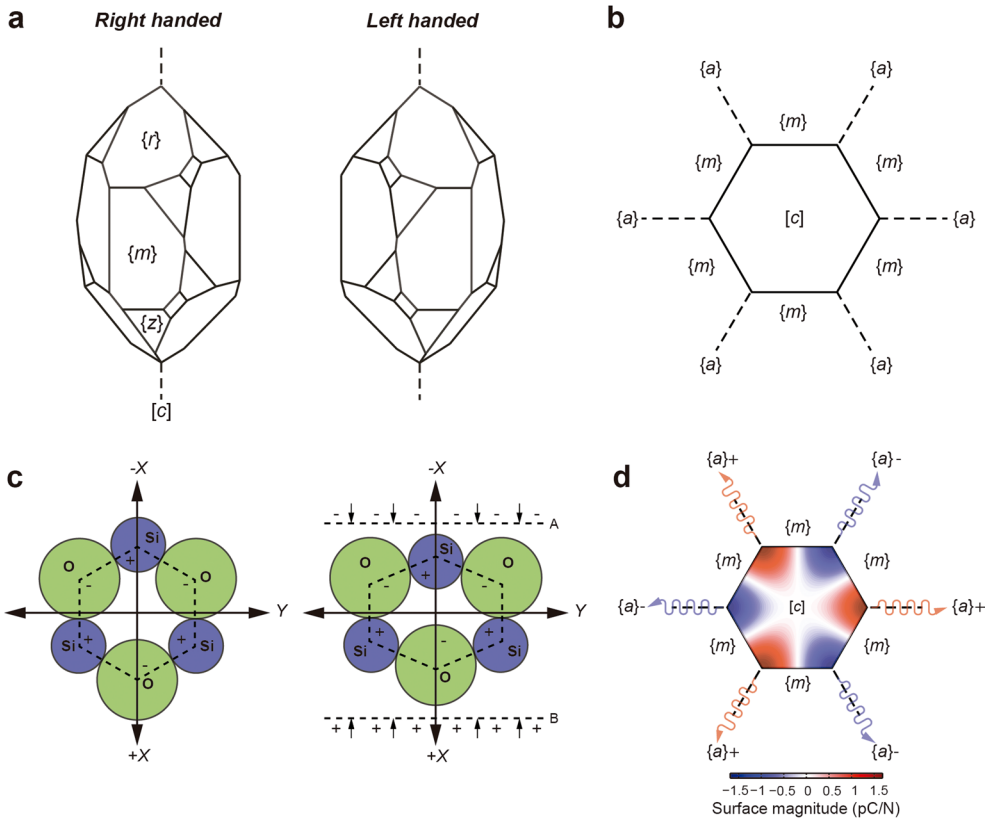

Extended Data Fig. 1 | The crystallography of quartz and related piezoelectric effects. The crystal planes of quartz and the piezoelectric response when distorted. (**a**) Crystallography of left- and right- handed quartz. The basal {c}, prismatic {m} and rhombohedral {r, z} planes are indicated. Minor planes, such as bipyramidal and acute rhombohedral, are not shown. (**b**) Quartz crystal viewed parallel to the c-axis. Here, the first- {m} and second- order {a} prismatic planes can be easily distinguished. (**c**) The effect of an applied mechanical stress (parallel to X) on the quartz atomic framework (top left and right). As the framework is distorted (top right), a piezoelectric potential is generated. When a quartz crystal is viewed parallel to the c-axis (bottom left and right) the distribution of positive (red) and negative (blue) piezoelectric charge can be recognised. (**d**) Note that only the {a} crystal planes are piezoelectric in quartz.

https://doi.org/10.1038/s41561-024-01514-1

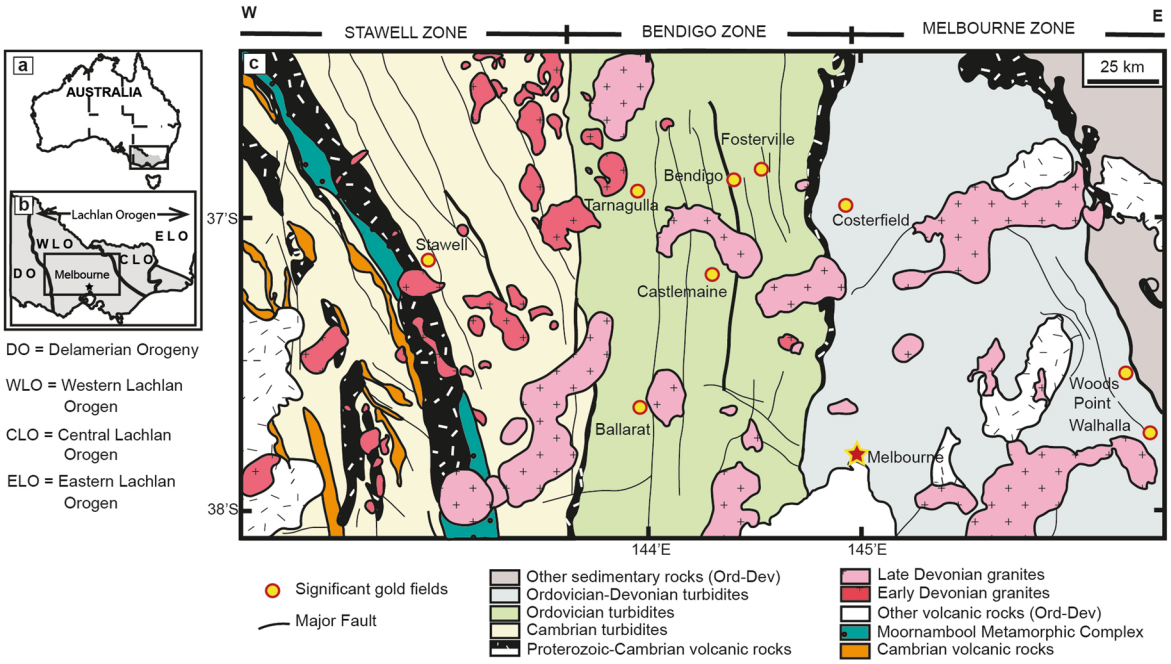

Extended Data Fig. 2 | Geological map of the Victorian goldfields, Australia. Major gold deposits in the Victorian goldfields, including the Fosterville deposit where samples for this study were sourced, from Voisey et al. (2020). (**a**) Schematic of Australia with the state of Victoria highlighted in grey. Position of (**b**) is indicated. (**b**) Inset map of Victoria and part of New South Wales showing the locations of the Lachlan orogen and the Delamerian orogen. Position of (**c**) is indicated. (**c**) Simplified geologic map of central Victoria, modified from Phillips et al. (2012). Infilled circles show major gold fields.

https://doi.org/10.1038/s41561-024-01514-1

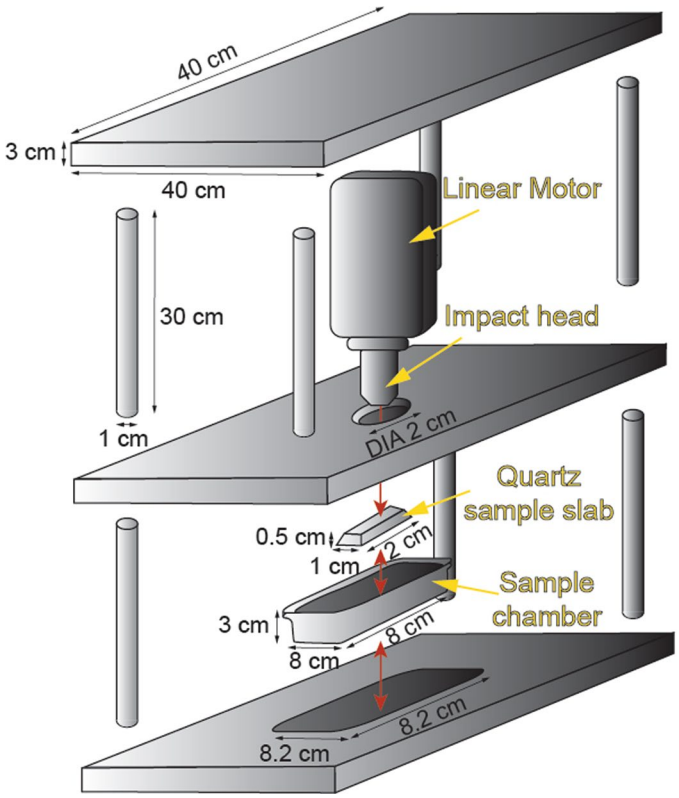

Extended Data Fig. 3 | Schematic of the apparatus used in all experiments. Deformation apparatus used in our experiments. The 2 x 1 x 0.5 cm quartz slab(s) are placed within an 8 x 8 x 3 cm sample chamber and submerged in 75 ml of gold-bearing solution. The perimeter of the sample chamber is sealed with silicon and the bottom plate has a trough to keep the sample chamber in place. Pressure is applied between the bottom two plates to prevent vertical bouncing during experimental oscillations. The quartz is then deformed by the actuator impact head for 1 hour at room temperature.

https://doi.org/10.1038/s41561-024-01514-1

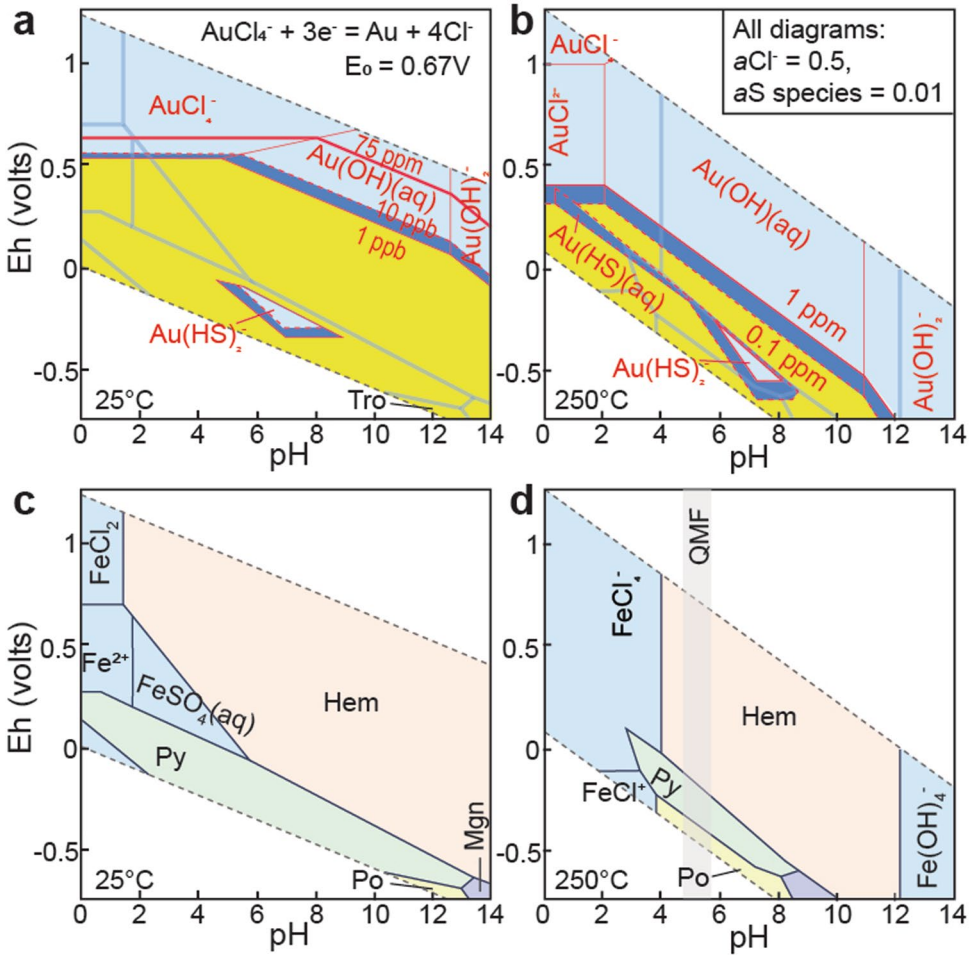

Extended Data Fig. 4 | Gold solubility in our experiments vs. typical orogenic systems. Eh vs. pH diagrams showing the potentials required to reduce aqueous gold. (**a**) Gold present as $AuCl_4^-$ in our room-temperature experiments and (**b**) shown as the $Au(HS)_2^- \pm Au(HS)(aq)$ complexes typical in orogenic gold fluids, into metallic gold, as a function of gold in solution. The diagrams of iron also shown for comparison, where (**c**) and (**d**) correspond to (**a**) and (**b**), respectively. Abbreviations: Hem – hematite, Mgn – magnetite, Po- pyrrhotite, Py – pyrite. QMF in (**d**) shows the pH corresponding to quartz-muscovite-K-feldspar for activities of K^+ of 0.1 to 0.01.

https://doi.org/10.1038/s41561-024-01514-1

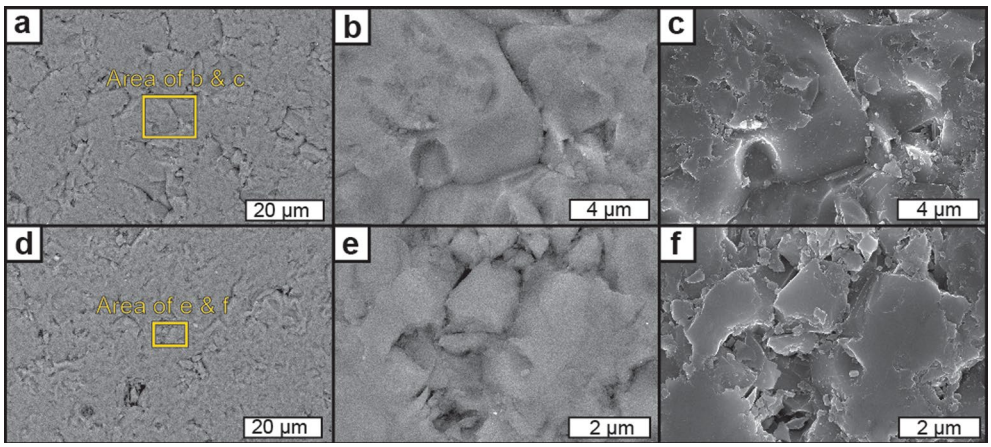

Extended Data Fig. 5 | Control results from uncoated quartz experiments. Imagery of the quartz crystal control slabs from our uncoated experiments. Samples were submerged in their respective solutions, but not deformed. (**a**) BSE image of bare quartz gold chloride (AuCl4) experiment. (**b**) and (**c**) are BSE and SE images, respectively, of the square area outlined in (**a**). (**d**) BSE image of bare quartz gold nanoparticle (AuNP) experiment. (**e**) and (**f**) are BSE and SE images, respectively, of the square area outlined in (**d**). BSE: Backscattered electron. SE: Secondary electron.

https://doi.org/10.1038/s41561-024-01514-1

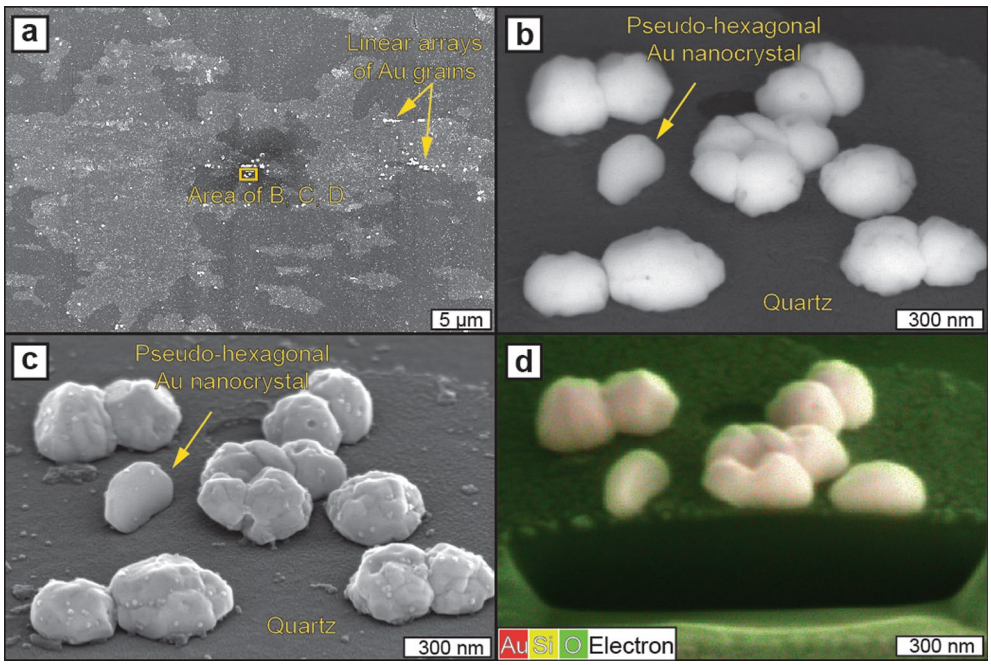

Extended Data Fig. 6 | Results from Ir-coated quartz with gold chloride ($AuCl_4$) experiment. Imagery of the Ir-coated quartz crystal slab after deformation within $AuCl_4$ solution. (**a**) BSE image of the quartz surface exhibiting distribution of gold particles deposits from $AuCl_4$ solution. Linear arrays, or 'branches', of gold particles can be seen. (**b**) and (**c**) are BSE and SE images, respectively, of the square area outlined in (**a**). Coupling of gold particles is evident as well as a pseudo-hexagonal Au nanocrystal. (**d**) EDS image of the square area in (**a**) highlighting the chemistry of sample area. BSE: Backscattered electron. SE: Secondary electron. EDS: Energy dispersive spectroscopy.

https://doi.org/10.1038/s41561-024-01514-1

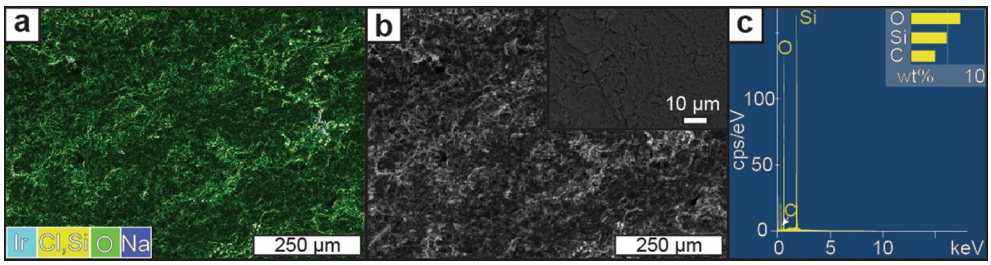

Extended Data Fig. 7 | Control results from from Ir-coated quartz with gold chloride ($AuCl_4$) experiment. Imagery of the Ir-coated quartz crystal control slab for the $AuCl_4$ solution experiment. Sample was submerged but not deformed. (**a**) EDS image of the quartz control sample surface. (**b**) BSE image of the quartz control sample surface. Inset shown at higher magnification. (**c**) EDS spectra of area in (**a**). BSE: Backscattered electron. EDS: Energy dispersive spectroscopy.

https://doi.org/10.1038/s41561-024-01514-1

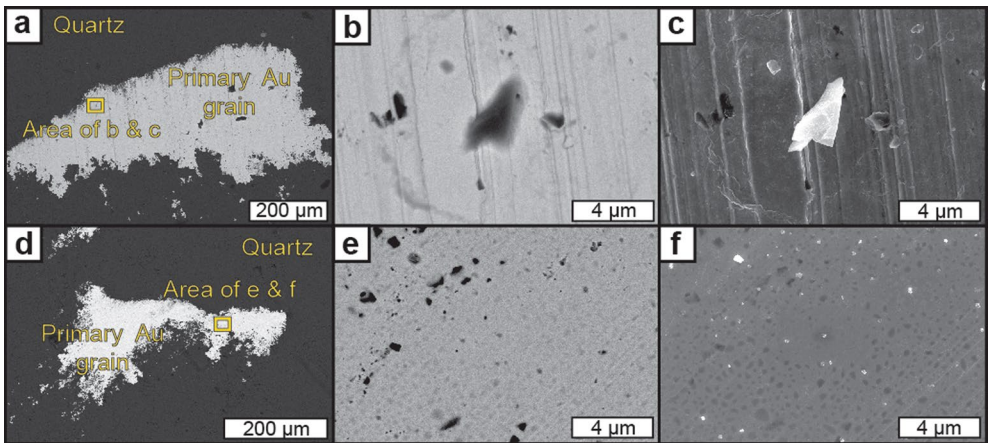

Extended Data Fig. 8 | Control results from natural auriferous quartz experiments. Imagery of the natural gold-bearing quartz control slabs from our growth experiments. Samples were submerged in their respective solutions, but not deformed. (**a**) BSE image of natural auriferous quartz gold chloride (AuCl4) experiment. Gold grain within quartz. (**b**) and (**c**) are BSE and SE images, respectively, of the square area outlined in (**a**). (**d**) BSE image of natural auriferous quartz gold nanoparticle (AuNP) experiment. Gold grain within quartz. (**e**) and (**f**) are BSE and SE images, respectively, of the square area outlined in (**d**). In both samples, particles seen on the gold grain surface are pieces of quartz. BSE: Backscattered electron. SE: Secondary electron.

https://doi.org/10.1038/s41561-024-01514-1

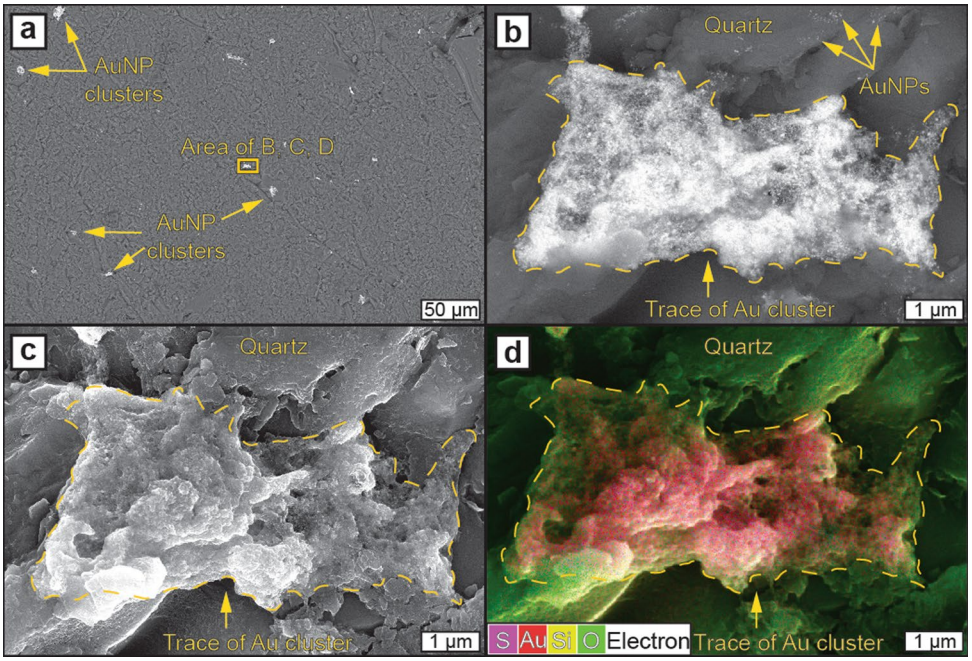

Extended Data Fig. 9 | Results from Ir-coated quartz gold nanoparticle (AuNP) experiment. Imagery of the Ir-coated quartz crystal slab after deformation within AuNP solution. (**a**) BSE image of the quartz surface exhibiting distribution of gold particles deposits from AuNP solution. Large clusters of AuNPs can be seen. (**b**) and (**c**) are BSE and SE images, respectively, of the square area outlined in (**a**). (**d**) EDS image of the square area in (**a**) highlighting the chemistry of sample area. BSE: Backscattered electron. SE: Secondary electron. EDS: Energy dispersive spectroscopy.

https://doi.org/10.1038/s41561-024-01514-1

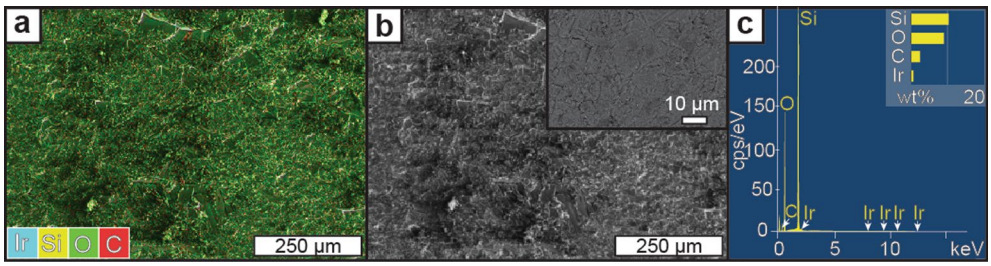

Extended Data Fig. 10 | Control results from Ir-coated quartz with gold nanoparticle (AuNP) experiment. Imagery of the Ir-coated quartz crystal control slab for the AuNP solution experiment. Sample was submerged but not deformed. (**a**) EDS image of the quartz control sample surface. (**b**) BSE image of the quartz control sample surface. Inset shown at higher magnification. (**c**) EDS spectra of area in (**a**). BSE: Backscattered electron. EDS: Energy dispersive spectroscopy.